

Nonlinear hydrodynamic analysis of an offshore oscillating water column wave energy converter

Yu Zhou^a, Dezhong Ning^{a,*}, Dongfang Liang^{a,b}, Shuqun Cai^{c,d}

^a State Key Laboratory of Coastal and Offshore Engineering, Dalian University of Technology, Dalian, 116024, China

^b Department of Engineering, University of Cambridge, Cambridge, CB2 1PZ, UK

^c State Key Laboratory of Tropical Oceanography, South China Sea Institute of Oceanology, Chinese Academy of Sciences, Guangzhou, 510301, China

^d Institution of South China Sea Ecology and Environmental Engineering, Chinese Academy of Sciences, China



ARTICLE INFO

Keywords:

OWC
WEC
Hydrodynamic performance
Boundary element method
Wave structure interaction

ABSTRACT

The hydrodynamic performance of a floating cylindrical oscillating water column (OWC) wave energy converter is investigated experimentally and numerically. The physical experiment is carried out in a wave flume at Dalian University of Technology. The floating cylindrical OWC device is constrained by springs and only moves vertically. A second-order time-domain Higher-Order Boundary Element Method, based on the perturbation expansion technique, is used to simulate the nonlinear wave interaction with the floating OWC device. The nonlinear terms concerning the pneumatic and viscous damping are introduced to the free surface boundary conditions inside the OWC chamber. The chamber surface elevation and air pressure, the hydrodynamic efficiency, and the vertical displacement of the OWC device are examined in detail. Good agreements are obtained between experimental data and numerical results. Then, the effects of opening ratio, wave steepness, mooring stiffness and chamber draft on the hydrodynamic performance are then investigated. It is found that the optimal opening ratio is between 0.02 and 0.03. The mooring stiffness plays an important role on the hydrodynamic response of the OWC device. The hydrodynamic efficiency and effective frequency bandwidth increase with the mooring stiffness.

1. Introduction

Renewable energy is an important step to overcome difficulties caused by the depletion of traditional energy resources and climate change [1]. Ocean energy has a high power density and great potential [2]. For centuries, a wide variety of WEC devices have been proposed and studied to utilize wave power [3,4]. Among them, the OWC-type WEC is the most attractive and extensively-studied one due to its simple structure and reliable technology [5]. The OWC WECs comprise a fixed or floating hollow structure and a water column inside the device [6]. The pneumatic air movement, which is induced by the motion of the water column, produces electrical energy with an air turbine [7]. The investigation of the OWC device has attracted worldwide attention, and a lot of prototype models have been tested in real-world marine environments [8]. Three different floating OWC devices (i.e., Sloped Buoy, Backward Bent Ducted Buoy and Spar Buoy) were tested in Atlantic environment in 2005 [9]. The Spar Buoy is considered to be the lowest-risk and most-economic OWC device [10]. A bottom-standing

OWC device (500 kW) was constructed on the shoreline of Jeju Island, South Korea in 2014 [11]. However, the OWC-type device is still not at the commercial-development stage [12].

A large number of OWC configurations have been proposed and studied, including fixed and floating structures [13]. Pawitan et al. [14] modelled a two-dimensional (2D) shoreline OWC device and predicted the wave loads on the front wall, the rear wall and the chamber ceiling. It is found that the vertical load has a significant influence on the stability of the OWC device. Ning et al. [15] carried out an experimental investigation on the hydrodynamic performance of a land-based dual-chamber OWC energy converter. The dual-chamber design can enhance the hydrodynamic efficiency of the OWC energy converter. Based on the experimental results, a numerical model is developed to design a U-type OWC wave energy converter with a dielectric elastomer generator [16]. The construction cost of the U-type OWC device is greatly reduced by sharing a common infrastructure with a breakwater. Based on Navier-Stokes equations, Xu et al. [17] applied a CFD numerical model to simulate the hydrodynamics of a circular bottom-sitting OWC device, which shows that the spatial non-uniformity inside the OWC chamber

* Corresponding author.

E-mail address: dzning@dlut.edu.cn (D. Ning).

Nomenclature	
<i>Notation</i>	
A	Incident wave amplitude
A_χ	Normalized amplitude error
b_w	Thickness of the chamber wall
b	Width of the flume
B	Viscous damping matrix
C	Hydro-restoring matrix
d	Draft of the OWC chamber wall
d_c	Air chamber height
$D=2R$	External diameter of the OWC chamber
D_o	Turbine diameter
f_m	Nonlinear terms connected with the dynamic response
f'_m, f''_m	Forcing terms on the still free surface boundary
$F^{(m)}$	m th order total wave force
F_m	Ramp function
F_{air}	Air pneumatic force
g	Gravitational acceleration
G	Green function
h	Water depth
H	Rotational matrix
k	Incident wave number
K	Stiffness matrix
K_s	Spring stiffness
m	Order of approximation
M	Mass matrix
$n = (n_x, n_y, n_z)$	Normal vector
p_s	Source point
P_{air}	Air pressure
P_{crest}	Crest amplitude of the air pressure
P_{trough}	Trongh amplitude of the air pressure
ΔP_{air}	Amplitude of the air pressure
P_{owc}	Extracted wave power
P_{inc}	Averaged incident wave energy
q_f	Field point
Q	Air volume flux
r_o	Inside radii of the damping layer
r_i	Outside radii of the damping layer
R_0	Distance between field point and Rankine source
R_z	Distance between field point and image of Rankine source
S	Boundary surface
S_0	Turbine cross-sectional area
S_B	Mean wet body surface
S_D	Seabed
S_f	Chamber cross-sectional area
S_{IF}	Chamber free surface
S_{OF}	Free surface outside the chamber
t	Time
T	Incident wave period
T^{nature}	Natural period
T_m	Ramp time
u	Air flow velocity through the turbine orifice
$u_c(t)$	Normal vertical velocity of chamber free surface
(x_r, y_r, z_r)	Rotational center coordinates
z	Vertical coordinate
Z_0	Initial displacement
ω	Angular frequency
ρ	Water density
φ	Spatial potential
φ_i	Incident potential
φ_s	Scattered potential
ϕ_χ	Normalized phase-amplitude error
$\eta_s^{(m)}$	m th order scattered wave elevation around the OWC
η_{crest}	Crest amplitude of the free surface
η_{trough}	Trongh amplitude of the free surface
$\Delta \eta_a$	Averaged surface elevation
λ	Wave length
μ_1	Artificial damping coefficient
μ_2	Nonlinear pneumatic damping coefficient
$\nu_{(r)}$	Damping coefficient of the damping layer
α_s	Solid angle coefficient
τ	Air flow damping coefficient
v	Viscous scale factor
ε	Opening ratio
$\partial/\partial n$	Normal derivative on the solid surface
ξ	Hydrodynamic efficiency
(ξ_1, ξ_2, ξ_3)	Body displacements of the surge, sway and heave
$(\alpha_1, \alpha_2, \alpha_3)$	Rotational displacements of the roll, pitch and yaw

can be enhanced by vortex shedding. Zheng et al. [18] performed an analytical study of an array of OWC devices, which are semi-embedded in a coastal structure. The interaction between the OWC array and the coastal structure significantly enhances the hydrodynamic properties of the OWC devices. The integration of the OWC wave energy converters into breakwaters contributes to reducing construction costs [19].

However, the construction of the onshore fixed OWC device is highly susceptible to coastal geometry. Moreover, the density of the wave energy is smaller near the shoreline than that in the deep sea. Deep-sea wave energy has drawn worldwide attention because of its high power intensity. Many floating OWC wave energy converters have been proposed and tested for operation in the deep sea [20]. Gomes et al. [21] studied the dynamics and power extraction of a heaving floating Spar-buoy OWC device in a wave flume, and showed that the flume wall can enhance the ability of energy capturing in both regular and irregular wave conditions. Based on the linear potential flow theory, Gomes et al. [22] further simulated the dynamics of a slack-moored Spar-buoy OWC device. Oikonomou et al. [23] performed a comparative study between an array of moored Spar-buoy OWC wave energy converters and an isolated device. The array layout is economic by sharing common mooring cables. Elhanafi et al. [24] used experimental and numerical methods to simulate the hydrodynamics of a cable-moored OWC wave

energy converter. The result shows that a large damping can improve the hydrodynamic efficiency in a low-frequency situation. Sheng [25] investigated the power performance of the backwards-bent duct buoy (BBDB) OWC wave energy converter. The motions of the BBDB OWC device, including the surge, heave and pitch modes, all contribute to energy conversion. Howe et al. [26] studied the hydrodynamic response of a Bent Duct OWC device integrated into a breakwater by the Finite Element Method (FEM). Compared with an isolated device, the capture efficiency of the OWC device increases significantly. Although there have been numerous studies on offshore OWC devices, the understanding of the complicated hydrodynamic interaction between nonlinear waves and the floating OWC device remains limited. Especially, the investigation on the effect of mooring stiffness on the hydrodynamic performance of the OWC device is still scarce. The present study considers a floating-moored cylindrical OWC device constrained in the heave mode. A systematic study and optimization are carried out to guide the geometrical design of the offshore OWC device.

A lot of methods have been used to model the complex interaction between waves and the OWC device [27]. Based on the linear wave theory and matched eigenfunction expansion technology, He et al. [28] developed an analytical model to optimize the geometrical parameters of an OWC device integrated into a pile-supported breakwater. The OWC

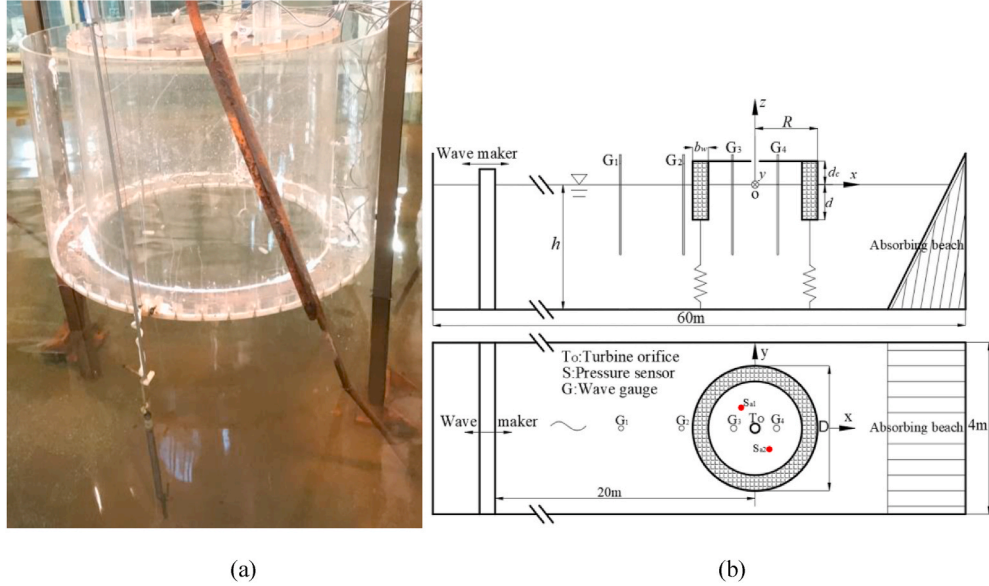


Fig. 1. Experimental setup (a) Photographs of the floating OWC device and (b) Sketch of the experimental setup.

device with a large back-wall draft can increase the hydrodynamic efficiency and decrease wave transmission. Zheng et al. [29] developed an analytical model to simulate an OWC device integrated into a vertical tubular structure. It is found that a thinner OWC chamber wall can lead to a broader effective frequency bandwidth. Following the linear wave theory and FEM, Nader et al. [30] analyzed the effects of array arrangement on the OWC devices. Due to the interaction between the OWC devices, the array enhances the overall power extraction and effective frequency bandwidth. However, the linear wave theory fails to simulate the real sea condition, including the effects of nonlinearity and viscosity [31,32]. A large number of experimental investigations have been undertaken to simulate the energy conversion of the OWC device in scaled physical models [33]. Singh et al. [34] experimentally studied the chamber wave elevations, air pressure and dynamic response of a floating moored OWC device. Ning et al. [35] performed an experimental study on an offshore dual-chamber OWC device subject to regular waves. Two different resonant frequencies were found for the dual-chamber OWC device. An experimental investigation with a scale of 1:20 is carried out to study the effects of spacing on an OWC array integrated into a detached breakwater [36]. Due to the three-dimensional (3D) effects, the absorbed power can be 2.2 times the incident wave power at resonance. Recently, a large number of CFD models, based on the Navier-Stokes (N-S) equations, have been developed to design the OWC device. Shalby et al. [37] built an incompressible 3D CFD model to simulate a fixed Multi-Chamber OWC device. The CFD results are found to be in good agreement with experimental data. Based on Reynolds Average Navier Stokes (RANS) method, Dai et al. [38] studied the effect of the model scale. The hydrodynamic scaling effect is linked to the Reynolds number. Simonetti et al. [39] used a compressible two phases CFD model to evaluate the effects of air compressibility on the performance of a fixed OWC device. The air pressure in the OWC chamber is overestimated by up to 15% when neglecting the air compressibility. Connell et al. [40] used a software package ANSYS Fluent to simulate a free heaving OWC spar buoy device with a non-linear Power Take-Off (PTO) system. However, the CFD simulations consume high computing resource, especially when dealing with a 3D OWC model. As a result, the Boundary Element Method (BEM) has been widely applied. Base on the potential flow theory and mixed Eulerian-Lagrangian approach, Koo and Kim [41] applied a fully nonlinear numerical wave tank (NWT) to simulate a land-based 2D OWC device. Ning et al. [35] studied the hydrodynamic properties of a land-based dual-chamber OWC with a fully nonlinear BEM model and

achieved good predictions. Wang et al. [42] analyzed the nonlinear and viscous effects on the hydrodynamic performance of a fixed OWC device with a fully nonlinear NWT. However, all of the above BEM models are 2D, and the studied OWC devices are fixed.

The previous numerical analyses on the 3D OWC device are mainly limited to analytical and CFD methods. The analytical approach generally can not consider the nonlinear effect, while the CFD approach is time-consuming. The 3D nonlinear time-domain Higher-Order Boundary Element Method (HOBEM) model, with a good balance between accuracy and efficiency, has long been applied to dynamic analyses of floating platforms [43], but it has rarely been used to study the 3D floating OWC device. Therefore, a 3D nonlinear numerical model based on the HOBEM and potential theory is developed in the present study. The contribution of each harmonic wave component to the hydrodynamics of the offshore OWC device is investigated.

As an extension of the previous land-fixed and offshore-fixed OWC researches [14,32], this paper focuses on the study of the hydrodynamics of an offshore floating OWC device with both experimental and numerical methods. The primary objective is to provide general guidance on the optimum design of the offshore cylindrical OWC device, including the device geometry and the mooring stiffness. The effects of the mooring stiffness, wave nonlinearity, PTO damping and chamber draft are considered. The paper is organized as follows. Section 2 presents the experimental setup and method for obtaining the hydrodynamic efficiency. A 3D nonlinear time-domain HOBEM model is described in Section 3. The nonlinear pneumatic and artificial damping are introduced to represent the turbine and viscous damping, respectively, inside the OWC chamber. Section 4 compares the experimental and numerical results. Section 5 discusses the effects of the opening ratio, wave steepness, mooring stiffness and chamber draft on the hydrodynamics of the OWC device. Finally, conclusions are summarized in Section 6.

2. Physical experiment

2.1. Experimental setup

A physical model of an offshore OWC device, as shown in Fig. 1(a), is studied at a scale of 1:20 in a wave-current flume at the State Key Laboratory of Coastal and Offshore Engineering, Dalian University of Technology. The flume is 60 m in length and 4 m in width, with a maximum water depth of 2.5 m. In the present study, both the fixed and

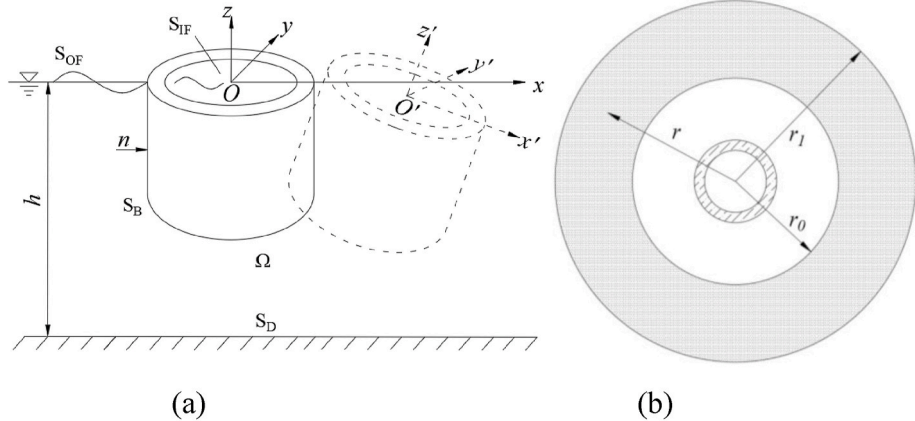


Fig. 2. Computational model: (a) the sketch of the floating OWC device, (b) the illustration of the sponge layer.

floating OWC devices are considered. The floating OWC device is constrained by two springs and moved only in the vertical direction. The sketch of the experimental setup is shown in Fig. 1(b). The OWC model is installed at the centre of the flume, 20 m away from the wave maker. The still water depth h is 1.0 m in all experimental cases. A Cartesian coordinate system $Oxyz$ is chosen with its origin at the centre of the OWC chamber and at the still water level, as shown in Fig. 1(b). The height of the OWC chamber d_c is set constant, i.e., 0.2 m. In the present scale-model tests, air compressibility can be neglected when ignoring the thermodynamic effects [44]. The chamber thickness b_w is 0.1 m, which provides sufficient buoyancy to the hollow device. The external diameter of the OWC chamber is $D = 2R = 0.8$ m. The effects of flume walls can be ignored with the ratio $b/D = 5$, where $b = 4$ m is the width of the flume [45]. A circular orifice with the diameter D_o is introduced to approximate the turbine damping at position T_0 (0 m, 0 m, 0.2 m) [35]. In the present study, four different opening ratios ε ($\varepsilon = 1.0\%, 1.5\%, 2.0\%$ and 3.0%) are considered to study the effects of turbine damping [46]. The opening ratio is defined as $\varepsilon = S_0/S_f$, where S_0 and S_f are the cross-sectional areas of the circular orifice and the circular chamber, respectively [47]. In the present study, two springs are used as mooring lines. Two different spring stiffness K_s (25 kg/m and 70 kg/m) are considered. Four resistive-type wave gauges (G_1 – G_4), with a sampling rate of 100 Hz, are deployed to measure the instantaneous free surface elevations at different locations, as indicated in Fig. 1(b). Wave gauge G_2 is fixed to the ground by a rigid support, which is used to measure the absolute wave runup in front of the OWC device at position G_2 (-0.525 m, 0 m, 0 m). The OWC chamber is fitted with two wave gauges at positions G_3 (-0.15 m, 0 m, 0 m) and G_4 (0.15 m, 0 m, 0 m). They are attached to the floating device, so that they can be used to easily measure the relative wave run-up elevation inside the OWC chamber. In order to measure the air pressure in the OWC chamber, two CY200-type pressure sensors, with a sampling rate of 100 Hz, are installed at positions S_{a1} (0.11 m, -0.11 m, 0.2 m) and S_{a2} (-0.11 m, 0.11 m, 0.2 m). An LXW-type draw-wire displacement sensor is installed directly above the floating OWC device to measure its vertical position. In the experiment, a series of waves are generated with four wave steepness $kA = 0.05, 0.075, 0.10$ and 0.015 , where A is the wave amplitude and k is the wave number.

2.2. Hydrodynamic efficiency

The hydrodynamic efficiency of the OWC device can be calculated as the ratio between the extracted pneumatic power and the incident wave power [48]. The time-averaged pneumatic power P_{owc} is calculated by integrating the product of the chamber air pressure P_{air} and the air volume flux Q [49] over time:

$$P_{owc} = \int_{S_f} \overline{P_{air}(t) \cdot Q(t)} dS = \frac{1}{T} \int_t^{t+T} P_{air}(t) \cdot S_f u_c(t) dt, \quad (1)$$

where T denotes the incident wave period, t is the time. $u_c(t)$ is the normal vertical velocity of the interior free surface, which can be calculated as:

$$u_c(t) = \dot{\eta}_a = \frac{1}{2} (\dot{\eta}_3(t) + \dot{\eta}_4(t)), \quad (2)$$

where η_3 and η_4 are the surface elevation at test points G_3 and G_4 , respectively, and the dot above the variable denotes the time derivative $\dot{\eta}(t) = d\eta(t)/dt = [\eta(t_2) - \eta(t_1)]/(t_2 - t_1)$.

The average energy flux per unit wave crest length P_{inc} is

$$P_{inc} = \frac{\rho g A^2 \omega}{4k} \left(1 + \frac{2kh}{\sinh 2kh} \right), \quad (3)$$

where g is the gravitational acceleration, ρ is the density of the water and ω is the angular frequency of the incident wave. Therefore, the hydrodynamic efficiency of the device can be defined as [50,51]:

$$\xi = \frac{P_{owc}}{P_{inc} \cdot 2(R - b_w)}, \quad (4)$$

where $2(R - b_w)$ in the denominator represents the internal diameter of the OWC chamber.

3. Numerical model

Based on the potential-flow theory, the second-order time-domain HOBEM model is applied to simulate the wave interaction with the floating OWC device [52]. Two cartesian coordinate systems are defined in Fig. 2(a). $X = (x, y, z)$ is fixed on the ground with its origin O . $X' = (x', y', z')$ is attached to the floating device with the origin O' , which is used to describe the hydrodynamic response of the OWC device. The two sets of coordinate systems coincide with each other as the OWC device is at its equilibrium position. The fluid is assumed to be inviscid and incompressible, and the flow irrotational. Then the fluid around the OWC device can be described by the complex velocity potential φ . The velocity potential is decomposed into the incident potential φ_i and the scattered potential φ_s [53]. The scattered potential φ_s satisfies the Laplacian equation:

$$\nabla^2 \varphi_s^{(m)} = 0 \quad (5)$$

where superscript m ($= 1$ & 2) denotes the order of approximations in satisfying the different nonlinear boundary conditions. Following the

second-order perturbation expansion procedure and the Taylor expansion method, the m th order impenetrable boundary condition on the wetted surface S_B for the scattered potential is:

$$\frac{\partial \varphi_s^{(m)}}{\partial n} = -\frac{\partial \varphi_i^{(m)}}{\partial n} + f_m \quad \text{on } S_B \quad (6)$$

where $\partial/\partial n$ denotes the derivative in the direction normal to the body surface, $\mathbf{n}=(n_x, n_y, n_z)$ is an outward unit vector, which points out to the fluid as shown in Fig. 2(a), f_m is the nonlinear terms related to the dynamic response of the OWC device and defined as:

$$f_1 = (\dot{\xi}^{(1)} + \dot{\alpha}^{(1)} \times (X - X_r)) \cdot \mathbf{n} \quad (7)$$

$$f_2'' = -\left(\frac{\partial \varphi_i^{(2)}}{\partial t} + g\eta_i^{(2)}\right) - \frac{1}{2}|\nabla \varphi^{(1)}|^2 - \eta^{(1)} \frac{\partial^2 \varphi^{(2)}}{\partial z \partial t} - \mu_1 \left(\eta^{(1)} \frac{\partial \varphi^{(1)}}{\partial n} + \frac{\partial \varphi^{(2)}}{\partial n}\right) \quad (16)$$

where μ_1 is the viscous damping coefficient which is used to model the effect of the fluid viscosity, $\eta^{(m)}$ denotes the m th total surface elevation, $\eta_i^{(m)}$ is the m th order incident wave. The viscous damping coefficients in the first and second-order dynamic boundary conditions are set the same for convenience. P_{air} denotes the air pressure in the OWC chamber, which can be related to the flow velocity [57]:

$$P_{air}(t) = \tau |Q(t)|Q(t) = \mu_2 |u(t)|u(t), \quad (17)$$

$$f_2 = n \cdot \left\{ \left(\dot{\xi}^{(2)} + \dot{\alpha}^{(2)} \times (X - X_r) \right) + \dot{H}(X - X_r) - \left[(\xi^{(1)} + \alpha^{(1)} \times (X - X_r)) \cdot \nabla \right] \nabla \varphi^{(1)} \right\} \\ + (\alpha^{(1)} \times n) \cdot \left[(\dot{\xi}^{(1)} + \dot{\alpha}^{(1)} \times (X - X_r)) - \nabla \varphi^{(1)} \right] \quad (8)$$

where $\xi=(\xi_1, \xi_2, \xi_3)$ is the surge, sway and heave displacements, respectively. $\alpha=(\alpha_1, \alpha_2, \alpha_3)$ is the roll, pitch and yaw rotations about x, y and z axes, respectively, defined as positive in the clockwise direction. $X_r=(x_r, y_r, z_r)$ denotes the rotational centre. H is a rotational matrix determined by the first-order displacement as follows:

$$H = -\frac{1}{2} \begin{bmatrix} (\alpha_2^{(1)})^2 + (\alpha_3^{(1)})^2 & 0 & 0 \\ -2\alpha_1^{(1)}\alpha_2^{(1)} & (\alpha_1^{(1)})^2 + (\alpha_3^{(1)})^2 & 0 \\ -2\alpha_1^{(1)}\alpha_3^{(1)} & -2\alpha_2^{(1)}\alpha_3^{(1)} & (\alpha_1^{(1)})^2 + (\alpha_2^{(1)})^2 \end{bmatrix} \quad (9)$$

In order to simulate the wave motion over a long time, a sponge layer is designed to absorb the reflected waves from the object [54], as shown in Fig. 2(b). To consider the fluid viscosity inside the OWC chamber, a damping term is introduced to the dynamic free surface boundary condition [55]. Then, the m th order kinematic and dynamic boundary conditions at the free surface are given as [56]:

$$\frac{\partial \eta_s^{(m)}}{\partial z} = \frac{\partial \varphi_s^{(m)}}{\partial z} - f'_m - \nu_{(r)} \eta_s^{(m)} \quad (10)$$

$$\frac{\partial \varphi_s^{(m)}}{\partial t} = -g\eta_s^{(m)} + f''_m - \nu_{(r)} \varphi_s^{(m)} \quad (11)$$

where $\eta_s^{(m)}$ denotes the m th order scattered surface elevation around the OWC device and $\nu_{(r)}$ is the damping coefficient of the sponge layer. The damping coefficient $\nu_{(r)}$ is defined as:

$$\nu_{(r)} = \begin{cases} \omega \left(\frac{r - r_0}{\lambda} \right)^2 & r_0 \leq r \leq r_1 \\ 0 & r < r_0 \end{cases} \quad (12)$$

where r_0 and r_1 are the inside and outside radii of the damping layer, as shown in Fig. 2(b). Wave length λ represents the damping-layer length. f'_m and f''_m are the forcing terms at the still free surface, defined as:

$$f'_1 = 0 \quad (13)$$

$$f_2' = -\left(\frac{\partial \varphi_i^{(2)}}{\partial z} - \frac{\partial \eta_i^{(2)}}{\partial t}\right) + \frac{\partial \varphi^{(1)}}{\partial x} \frac{\partial \eta^{(1)}}{\partial x} + \frac{\partial \varphi^{(1)}}{\partial y} \frac{\partial \eta^{(1)}}{\partial y} - \eta^{(1)} \frac{\partial^2 \varphi^{(1)}}{\partial z^2} \quad (14)$$

$$f_1'' = -\frac{1}{\rho} P_{air} + \mu_1 \frac{\partial \varphi^{(1)}}{\partial n} \quad (15)$$

where τ is the air flow damping coefficient, u denotes the air flow velocity through the circular orifice, $\mu_2 = \tau S_0^2$ is the nonlinear pneumatic damping coefficient characterizing the turbine damping. Both μ_1 and μ_2 can be determined by fitting the experimental measurements. It should be noted that the effects of air pressure and fluid viscosity are only considered inside the OWC chamber.

The above-mixed boundary value problem can be solved by the BEM with the Rankine source and its image about the seabed [58]:

$$G(p_s, q_f) = -\frac{1}{4\pi} \left(\frac{1}{R_0} + \frac{1}{R_z} \right), \quad (16)$$

where $p_s = (x_1, y_1, z_1)$ and $q_f = (x, y, z)$ are the source point and field point, respectively, and

$$\begin{cases} R_0 = \sqrt{(x - x_1)^2 + (y - y_1)^2 + (z - z_1)^2} \\ R_z = \sqrt{(x - x_1)^2 + (y - y_1)^2 + (z + z_1 + 2h)^2} \end{cases}, \quad (17)$$

Then, the m th order integral equation for the scattered potential can be obtained:

$$\alpha_s \varphi_s^{(m)}(p_s) = \iint_S \left[\varphi_s^{(m)}(q_f) \frac{\partial G(q_f, p_s)}{\partial n} - G(q_f, p_s) \frac{\partial \varphi_s^{(m)}(q_f)}{\partial n} \right] ds, \quad (18)$$

where α_s is the solid angle coefficient, the boundary surface S includes the mean free surface (S_{OF} and S_{IF}) and the mean wet solid surface S_B . This integral equation can be discretized and solved numerically [53].

After solving the above integral equation, the m th order spatial potential can be obtained. Then, the m th order hydrodynamic response of the OWC device can be calculated from the following motion equations:

$$[M]\{\ddot{\xi}^{(1)}\} + [B]\{\dot{\xi}^{(1)}\} + ([C] + [K])\{\xi^{(1)}\} = \{F^{(1)}\} + \{F_{air}\} \quad (19)$$

$$[M]\{\ddot{\xi}^{(2)}\} + [B]\{\dot{\xi}^{(2)}\} + ([C] + [K])\{\xi^{(2)}\} = \{F^{(2)}\} \quad (20)$$

where M is the mass matrix, C is the hydro-restoring matrix, K is the structural stiffness matrix associated with the mooring system. B is the viscous damping matrix, which is expressed as $B=\nu M$ [59]. ν is the viscous scale factor, which can be determined by fitting the experimental measurements. $F^{(m)}$ is the m th order total wave force vector, F_{air} denotes the pneumatic force on the chamber wall. It should be noted that the contribution from the pneumatic force is only considered in the first-order analysis. In the time domain, the simulation is advanced using the fourth-order Adams-Bashforth predictor-corrector scheme and the

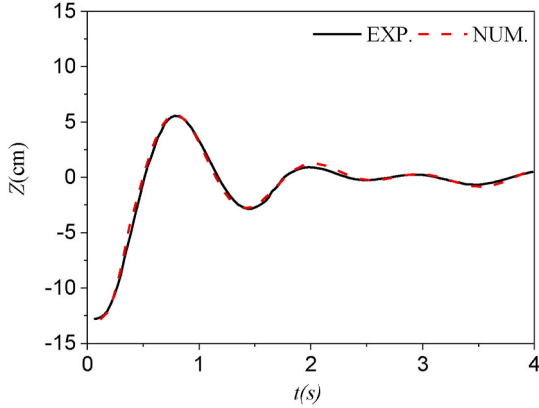


Fig. 3. Time series of the simulated and measured free decay test in heave motion.

fourth-order Runge-Kutta (RK4) scheme in calculating the free surface and the motion responses, respectively. In order to avoid impulsive phenomena at the beginning of the simulation, a ramp function is introduced to multiplying by the incident wave velocity or the object velocity in the forced motion simulation, which is expressed as:

$$F_m = \begin{cases} \frac{1}{2} \left[1 - \cos\left(\frac{\pi t}{T_m}\right) \right] & t \leq T_m \\ 1 & t \geq T_m \end{cases} \quad (23)$$

where T_m is the ramp time.

Then, the air volume flux $Q(t)$ can be expressed as:

$$Q(t) = \int_{S_f} \dot{\eta}(t) dS \quad (24)$$

where $\eta(t) = \eta_{real}(t) - \xi_3(t)$ is the relative water motion inside the OWC chamber.

4. Comparison between numerical and experimental results

In the present study, experimental results are used to validate the HOBEM model. The geometric parameters are kept the same as in the physical model, such as the device draft $d = 0.3$ m, the external diameter of the chamber $D = 0.8$ m and the chamber thickness $b_w = 0.1$ m. The water depth of the numerical model is set to be 1 m. In order to absorb

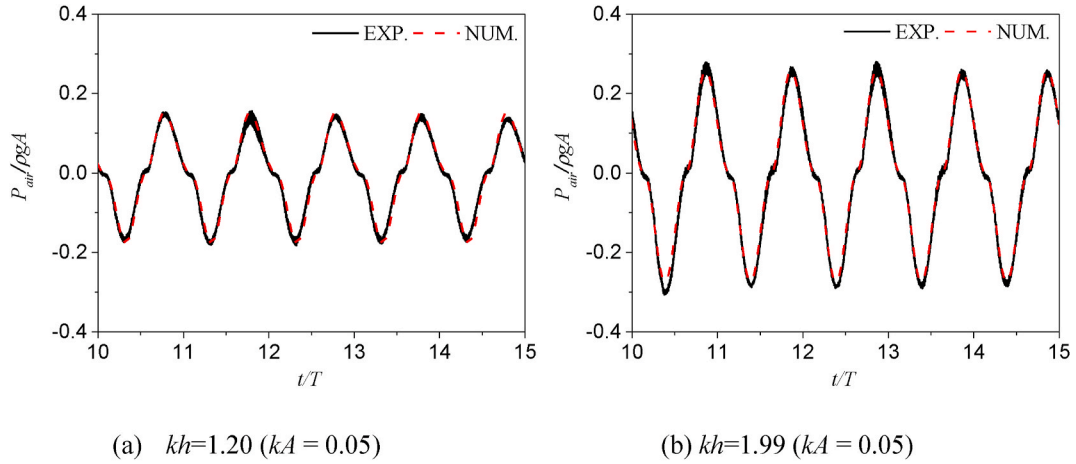


Fig. 4. Time series of the simulated and measured chamber air pressures in the stationary device with $\epsilon = 2.0\%$.

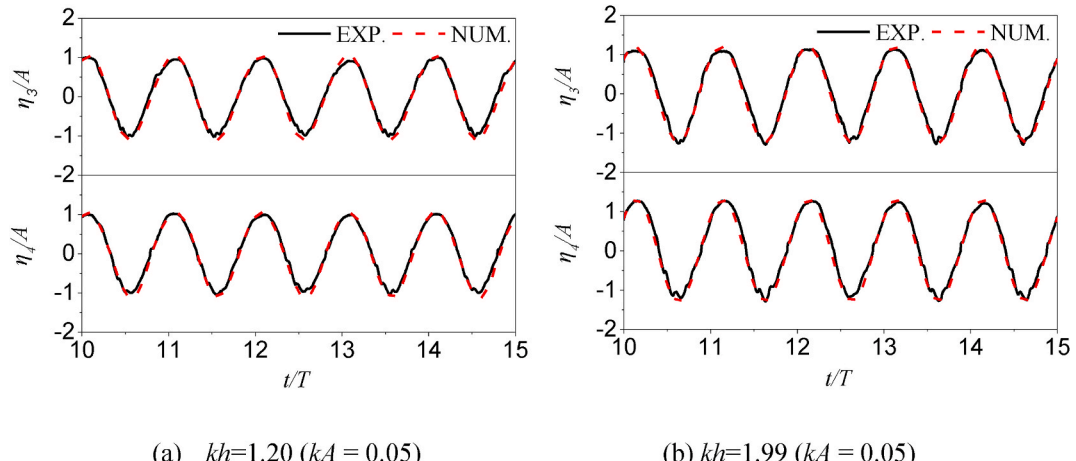


Fig. 5. Time series of the simulated and measured surface elevations at G_3 and G_4 in the stationary device with $\epsilon = 2.0\%$.

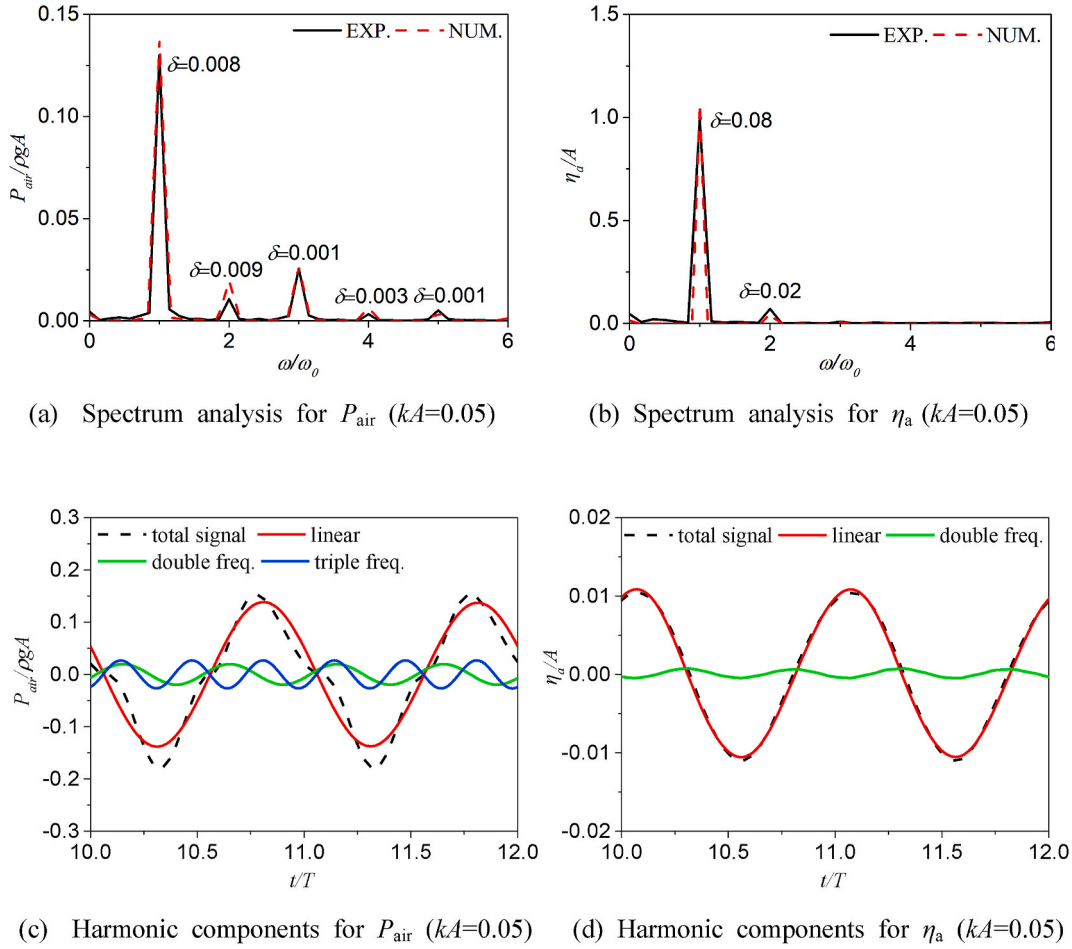


Fig. 6. Nonlinear analysis for air pressure P_{air} and averaged chamber surface elevation η_a at $kh = 1.2$ with $\epsilon = 2.0\%$.

the reflected waves at the far field, the sponge layer is introduced with the radii $r_1 = 2\lambda$ and $r_0 = \lambda$ as shown in Fig. 2(b). In the present time-domain numerical model, the time step Δt is specified to be $T/500$. After convergence tests, the computational domain is discretized into 588 nodes and 192 elements on the OWC device surface, and 1732 nodes and 492 elements on the free water surface. Each simulation is run for $30T$ on a laptop computer with eight Intel Core i5-8250U processors and usually takes about 6 min to complete.

A vertical free decay test is conducted to validate the accuracy of the HOBEM model firstly. The mass of the OWC model M_{33} is 67.45 kg. The diameter of the orifice is $D_o = 0.104$ m, and the draft of the OWC device d is 0.3 m in calm water. An external force is exerted on the experimental model in the vertical direction to enable an initial displacement $Z_0 = -12.5$ cm, and then the device is released. In the present numerical model, the controlling variables method is applied to determine the adaptable viscous scale factor v and the pneumatic damping coefficient μ_1 [47]. Firstly, the value of the μ_1 is set as zero, and the value of v is changed for a closest results for the experiment data. Then, the value of v is fixed as 0.8 and the value of μ_1 is varied. Finally, the viscous scale factor v and the pneumatic damping coefficient μ_1 are selected as 0.8 and 0.036, respectively. Fig. 3 shows the time series of the simulated and measured free decay test of the floating OWC device. It can also be seen that the vertical natural period of the floating OWC device T_3^{natural} is 1.2 s. The good agreement between the numerical and experimental results verifies the high accuracy of the present HOBEM model.

Further, the air pressure and surface elevation of the offshore stationary OWC chamber are presented. The diameter of the orifice is $D_o = 0.085$ m. Based on the trial and error procedure, the artificial and nonlinear pneumatic damping coefficients are chosen to be $\mu_1 = 0.015$

and $\mu_2 = 1.45$, respectively. Fig. 4 shows the time history of the air pressure P_{air} inside the chamber, while Fig. 5 shows the surface elevations at G_3 and G_4 . In these examples, kA is equal to 0.05, while the value of kh is either 1.20 or 1.99. Good agreement can be seen between the numerical and the experimental results. Besides, it can be seen that the long-term variations are well predicted using the limited numerical domain. It verifies the good performance of the present nonlinear HOBEM model.

In order to investigate the nonlinear effects, fast fourier transform (FFT) is used to investigate the harmonic decompositions of the air pressure P_{air} and the averaged water surface elevation $\eta_a = (\eta_3 + \eta_4)/2$ inside the OWC chamber. Figs. 6 and 7 show the spectrum analyses and the harmonic components of P_{air} and η_a at $kh = 1.2$ and 1.99, respectively. And, the residual values δ ($\delta = |\chi^{\text{num}} - \chi^{\text{exp}}|$, where χ represents the value of the quantity in concern) for each harmonic decompositions are also labeled. Figs. 6(a)–(b) and 7(a)–(b) indicate good agreements between the numerical simulations and experimental measurements. It can also be seen that the linear component is the dominant contribution to both the air pressure and the averaged surface elevation. As seen in Fig. 6(a), all five harmonic components, i.e., linear, double, triple, quadruple and penta frequency components, are necessary for accurately describing the air pressure variation. In Figs. 6(c) and 7(c), only the linear, double and triple frequency components of the air pressure are plotted for clarity. In contrast, only the first two harmonic components are necessary for accurately describing the chamber free surface oscillation. The higher-order harmonic components needed for the air pressure description are related to the effects of nonlinear waves and quadratic pneumatic damping as shown in Eq. (17). The odd-order harmonic components of the air pressure oscillations, i.e., linear, triple

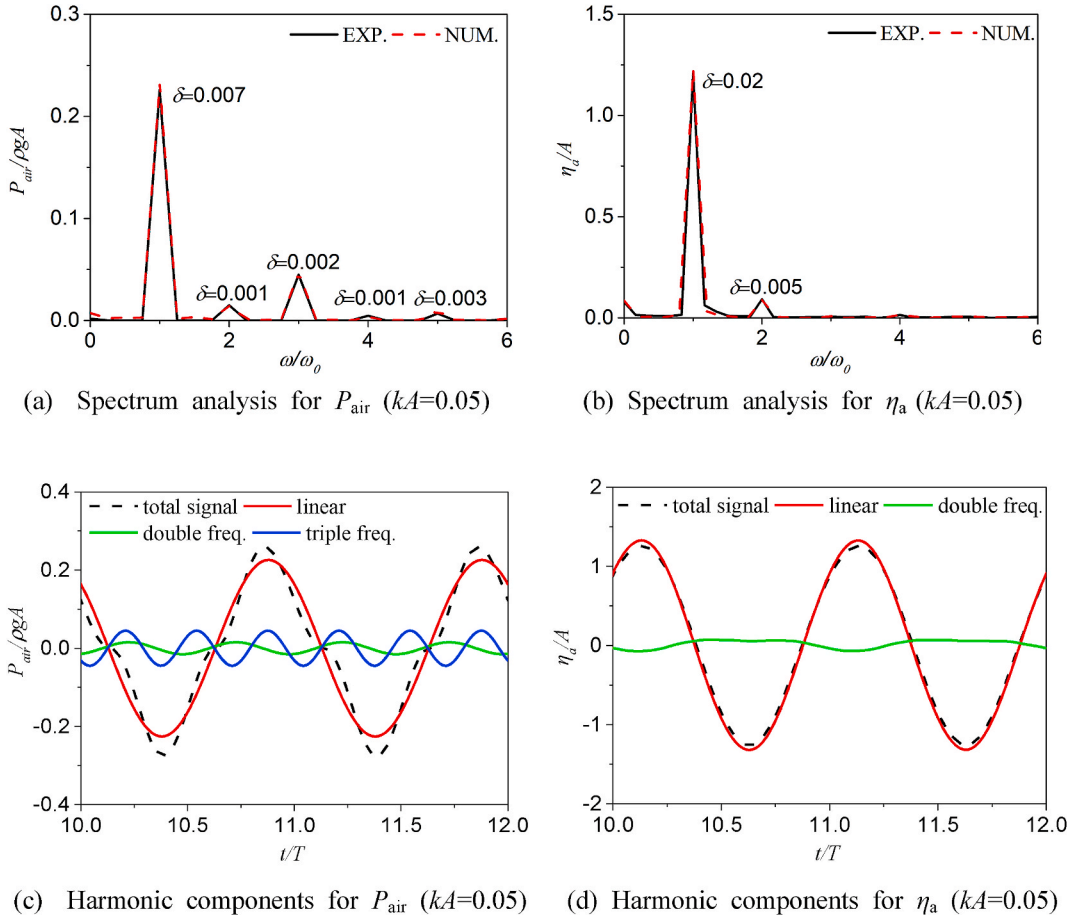


Fig. 7. Nonlinear analysis for air pressure P_{air} and averaged chamber surface elevation η_a for $at = 1.99$ with $\epsilon = 2.0\%$.

and penta frequency components, are induced by the linear waves, while the even-order harmonic components, i.e., double and quadruple frequency components, are induced by the second-order waves.

In order to validate the suitability of the artificial and pneumatic damping coefficients μ_1 and μ_2 , the higher nonlinear waves ($kA = 0.075$, 0.10 and 0.15) are considered while they interact with stationary OWC devices. Figs. 8 and 9 illustrate the time series of the air pressure P_{air} and the surface elevations at points G_2 , G_3 and G_4 . While changing the wave steepness kA , the water depth is kept the same $kh = 1.99$. It can be seen that the air pressure response is nonlinear, and the air pressure amplitudes are asymmetric for nonlinear waves. This is due to the effects of the second-order waves, which can enhance the chamber volume flow rate. From the figures, the predicted air pressure and surface elevation in the chamber show good agreements with the experimental data. It further illustrated that the present second-order HOBEM model can be used to simulate the WEC hydrodynamics in strong nonlinear waves.

In this paper, the normalized amplitude error A_χ and normalized phase-amplitude error ϕ_χ are considered for the quantitative evaluation of the agreement between the predicted and measured air pressure and surface elevation, which are expressed as [60]:

$$A_\chi = \sqrt{\frac{\sum_{i=1}^N (\chi_i^{\text{num}})^2}{\sum_{i=1}^N (\chi_i)^2}}; \quad \phi_\chi = \sqrt{\frac{\sum_{i=1}^N (\chi_i^{\text{num}} - \chi_i)^2}{\sum_{i=1}^N (\chi_i)^2}} \quad (25)$$

where N is the number of samples. A perfect agreement would result in $A_\chi \rightarrow 1$ and $\phi_\chi \rightarrow 0$. The normalized amplitude and phase-amplitude errors for the time series shown in Figs. 4–5 and 8–9 are listed in Tables 1 and 2, respectively. A good agreement between numerical and experimental results are evident, with $A_\chi \approx 1$ and $\phi_\chi \leq 0.09$.

5. Results and discussions

5.1. Effects of turbine damping

In this section, the effects of turbine damping on the hydrodynamic performance of the stationary OWC device are studied. In the experiment, four different opening ratios ($\epsilon = 1.0\%$, 1.5% , 2.0% and 3.0%) are considered with diameters $D_{o1} = 0.060$ m, $D_{o2} = 0.073$ m, $D_{o3} = 0.085$ m and $D_{o4} = 0.104$ m, respectively. The draft of the OWC device d is kept as 0.3 m. The external diameter of the OWC chamber is $D = 0.8$ m. The steepness of the incident wave is set at a constant $kA = 0.05$. The geometric and dynamic parameters of the HOBEM model are set the same as those in the physical model. The incident wave number, normalized by the water depth, is in the range of $1 \leq kh \leq 3$. The effects of the opening ratio ϵ on the amplitude of chamber air pressure $\Delta P_{air} = (P_{\text{crest}} - P_{\text{trough}})/2$ and the averaged surface elevation $\Delta \eta_a = (\eta_{\text{crest}} - \eta_{\text{trough}})/2$ are illustrated in Fig. 10. The opening ratio ϵ , which characterizes the turbine damping, has a great influence on the hydrodynamics of the OWC chamber. With the increase of the opening ratio ϵ , the surface elevation increases and the air pressure decreases. It is reasonable that the air pressure and the motion of the chamber surface elevation are negatively correlated. From Fig. 10, it can be seen that the resonant frequency occurs around $kh = 2.1$ in terms of both the air pressure and the averaged surface elevation. Following Eq. (17), a larger averaged surface elevation can lead to larger air pressure inside the OWC chamber. In the low frequency domain, the air pressure ΔP_{air} increases rapidly with the decrease of the opening ratio ϵ . However, the averaged surface elevation remains close to unity [61]. This is due to the long waves that can penetrate the OWC wall easily. The effect of air pressure on the surface elevation of the chamber can be ignored in the low frequency domain. Fig. 11 illustrates the

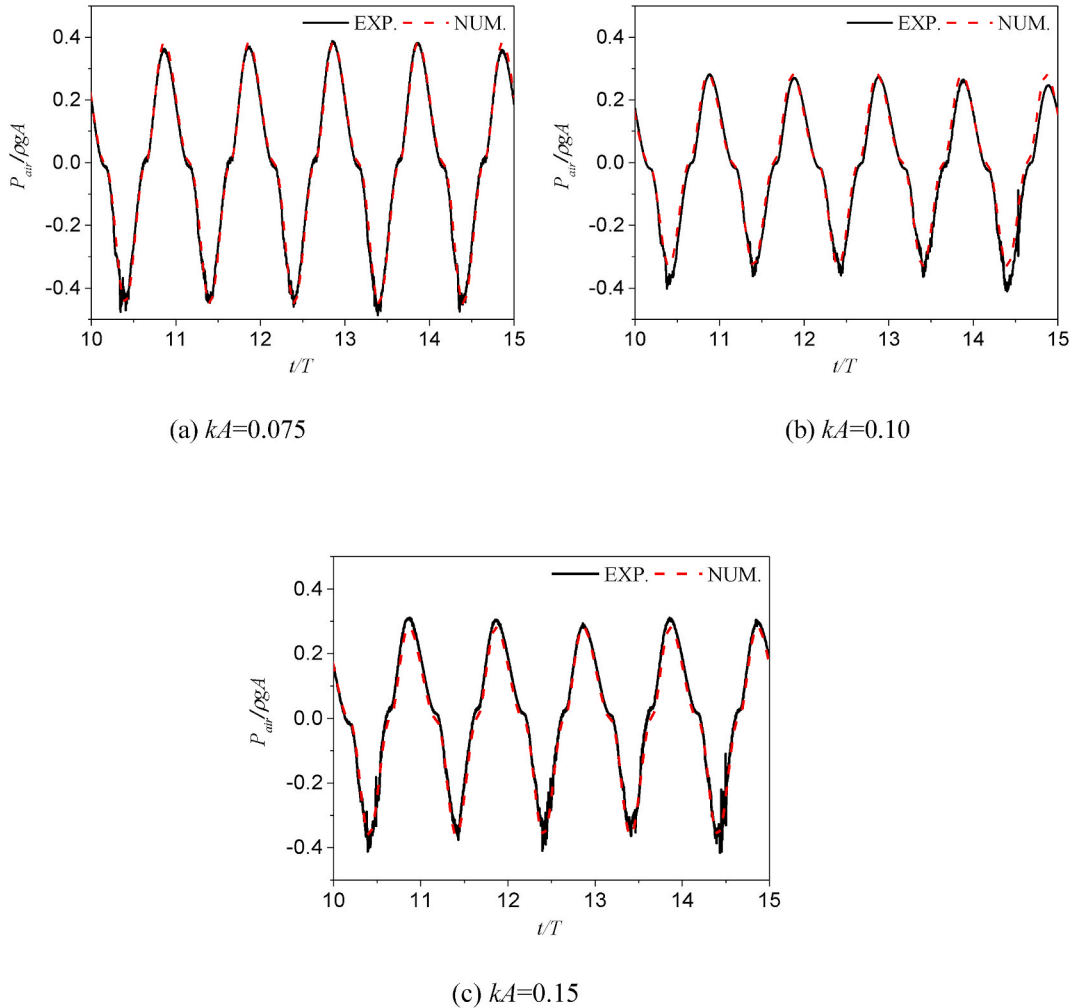


Fig. 8. Time series of the simulated and measured air pressure in the chamber at $kh = 1.99$ for three different wave steepness.

effects of the opening ratios ϵ on the hydrodynamic efficiency ξ with the horizontal axis as the dimensionless wave number kh . The maximum efficiency of the OWC device is found to be about 0.575 with $kh=2.1$ in Fig. 11. The maximum efficiency of the offshore device occurs at the same dimensionless wave number ($kh=2.1$) as the air pressure and chamber surface elevation [62]. The optimal opening ratio for the present OWC device is between 2% and 3%. A similar conclusion is also obtained in a small-scale physical test [63]. In Fig. 11, the dashed line marks the effective frequency bandwidth with the efficiency $\xi \geq 20\%$. It is found that, as the opening ratio ϵ increases, the effective frequency bandwidth of the OWC device decreases. Hence, a larger turbine damping is suggested to improve the hydrodynamic efficiency of the OWC device in both low and high frequency regions.

5.2. Effects of wave steepness

In this section, the effects of wave steepness kA on the hydrodynamic properties of the offshore stationary OWC device are discussed. In the present physical tests, three different higher nonlinear waves ($kA = 0.075, 0.10$ and 0.15) are considered in four wave conditions ($kh = 1.99, 2.11, 2.26$ and 2.6), which are used to validate the suitability of the HOBEM model for higher nonlinear waves. The experiment results for the wave steepness $kA=0.05$ are also discussed. The main geometric parameters are chosen as $d = 0.3$ m, $b_w = 0.1$ m and $D = 0.8$ m. The opening ratio ϵ is set as 2.0%. Apart from the experimental tests, the hydrodynamics of the OWC device with different wave steepness are also simulated by the HOBEM model, with a range of $1 \leq kh \leq 3$. The

artificial and nonlinear pneumatic damping coefficients are chosen to be $\mu_1=0.015$ and $\mu_2=1.45$, respectively.

Fig. 12 shows the effects of wave steepness kA on the non-dimensional amplitude of the chamber air pressure $\Delta P_{air}/\rho g A$ and averaged surface elevation $\Delta \eta_a/A$. It is clear that the measured and predicted results agree well. The non-dimensional amplitudes of the air pressure $\Delta P_{air}/\rho g A$ and the averaged surface elevation $\Delta \eta_a/A$ vary in opposite trends with wave steepness kA . The same resonant frequency ($kh = 2.1$) is found as the previous study, which illustrates the independence between wave steepness and resonant characteristics. In Fig. 12(a), the air pressure $\Delta P_{air}/\rho g A$ increases with wave steepness kA , especially for low frequencies. It can be explained by the rate of the surface variation $(\eta_{crest(t)}-\eta_{trough(t)})/T$ inside the chamber, which increases with the wave steepness kA . When the frequency is low, the long wave with stronger penetrability contributes to the increase of the air pressure, as shown in Fig. 12(a). Fig. 12(b) illustrates the effects of the wave steepness kA on the dimensionless surface elevation $\Delta \eta_a/A$. It can be seen that the dimensionless surface elevation decreases with the increase of the wave steepness, especially nearby the resonant frequency [47].

The spectral analyses of the averaged free surface elevation inside the chamber at $kh=2.11$ are shown in Fig. 13. In order to examine the influence of the wave steepness kA , four steepness values are considered. It is clear that the numerical and experimental results agree well. Although the third-order harmonic wave is visible in the experiment, the free surface oscillation is mainly dominated by the fundamental and second-order harmonic components. The comparison illustrates the

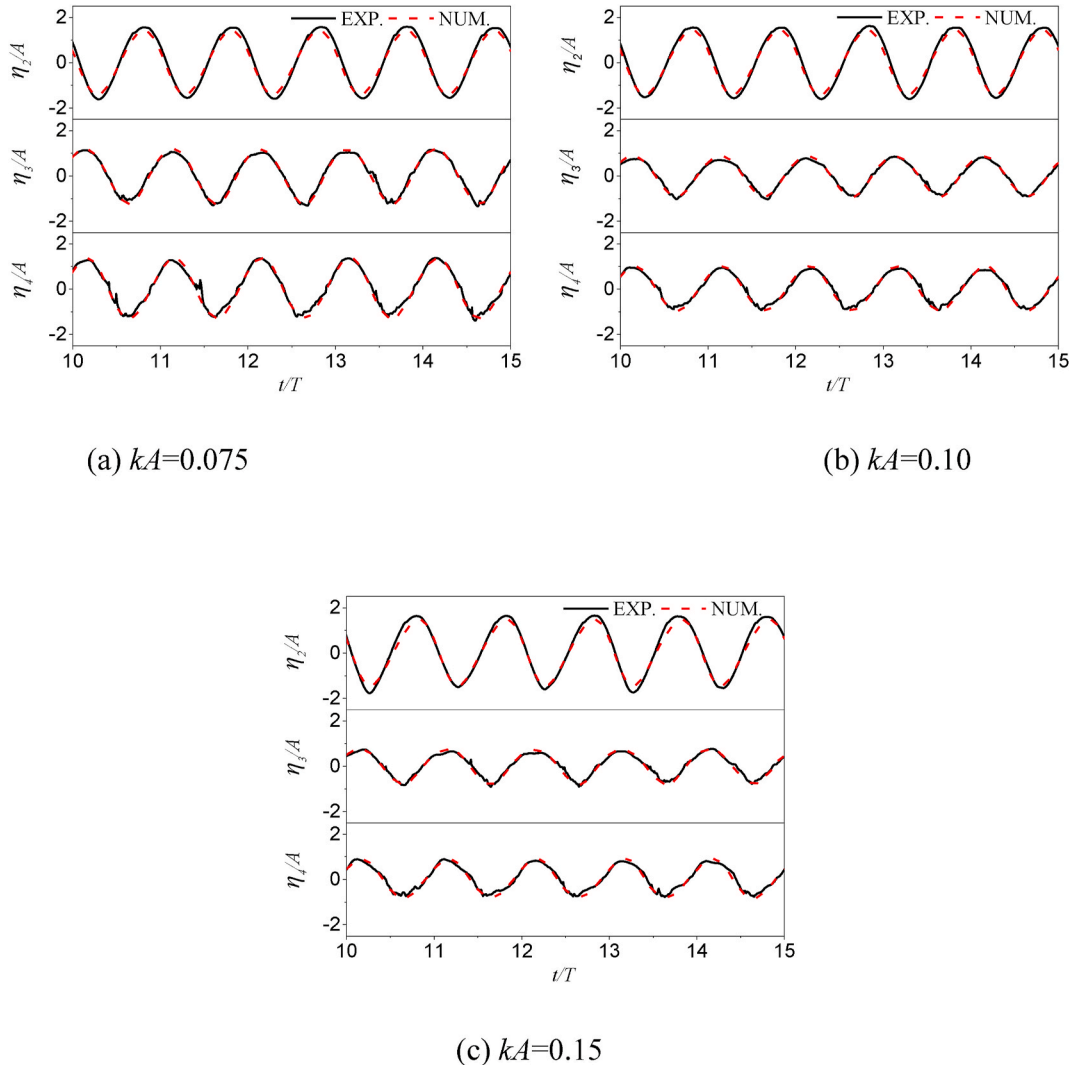


Fig. 9. Time series of the simulated and measured surface elevations at G_2 , G_3 and G_4 at $kh = 1.99$ for three different wave steepness.

Table 1

Normalized amplitude and phase-amplitude errors for air pressure and surface elevations with $kA=0.05$.

	P_{air}		η_3		η_4	
	A_χ	ϕ_χ	A_χ	ϕ_χ	A_χ	ϕ_χ
$kh=1.20$	1.03	0.03	1.07	0.08	1.08	0.09
$kh=1.99$	0.96	0.05	1.01	0.03	1.09	0.09

Table 2

Normalized amplitude and phase-amplitude errors for air pressure and surface elevations at $kh=1.99$.

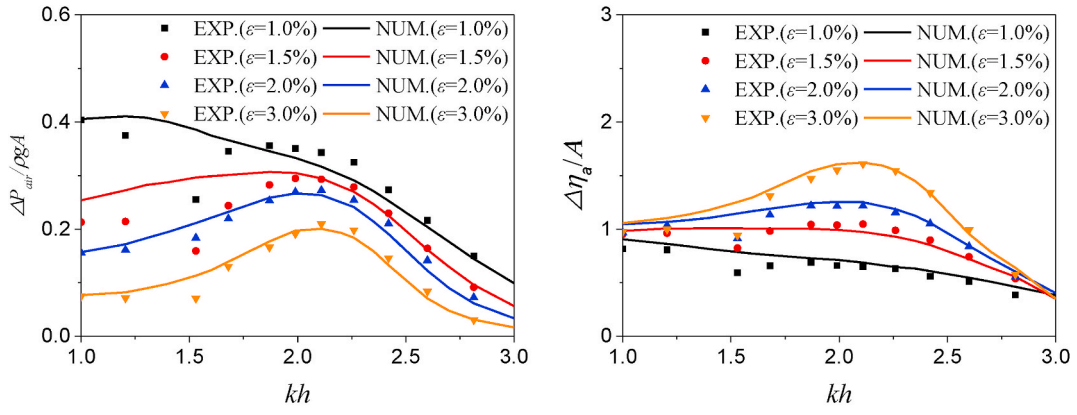
	P_{air}		η_2		η_3		η_4	
	A_χ	ϕ_χ	A_χ	ϕ_χ	A_χ	ϕ_χ	A_χ	ϕ_χ
$kA=0.075$	1.02	0.03	0.90	0.09	1.05	0.06	1.03	0.07
$kA=0.10$	1.05	0.07	0.92	0.08	1.08	0.09	1.04	0.05
$kA=0.15$	0.99	0.03	0.91	0.09	1.07	0.07	1.01	0.05

suitability of the HOBEM model for the hydrodynamic prediction of the nonlinear wave behaviour with steepness up to 0.15. Furthermore, the dimensionless resonance peak at the fundamental frequency is seen to decrease from 1.29 to 0.78 when the wave steepness kA increases from 0.05 to 0.15 [64]. The stronger nonlinear waves consist of many higher-order harmonics, which can be easily reflected by the OWC chamber wall. As a result, the relative surface elevation inside the OWC chamber decreases.

The variations of the hydrodynamic efficiency with wave steepness kA are shown in Fig. 14. In the low ($kh \leq 1.75$) and high ($kh \geq 2.5$) frequency regions, the hydrodynamic efficiency increase with the wave steepness kA . However, for intermediate frequency region ($1.75 \leq kh \leq 2.5$), the hydrodynamic efficiency decreases with the wave steepness kA . López et al. [65] and Kamath et al. [66] also observed the same trends in the study of a land-fixed OWC device. At the resonant frequency ($kh = 2.1$), the air pressure inside the chamber rises by 16.9% as kA increases from 0.05 to 0.15. However, the surface elevation decreases at a rate of about 38.4%, which is higher than the rate of the air pressure rise and thus explains the reduction of the hydrodynamic efficiency.

5.3. Effects of mooring stiffness

This section explores the effects of mooring stiffness on the hydrodynamic performance of the floating OWC device. A free-floating OWC



(a) Amplitude of the chamber air pressure (b) Amplitude of the averaged surface elevation

Fig. 10. Effects of the opening ratios ε on the hydrodynamic properties of the OWC chamber.

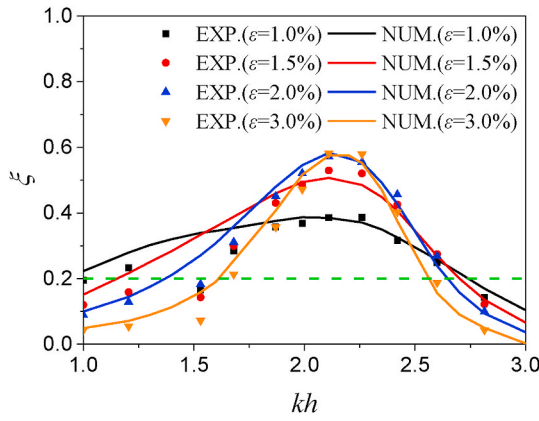
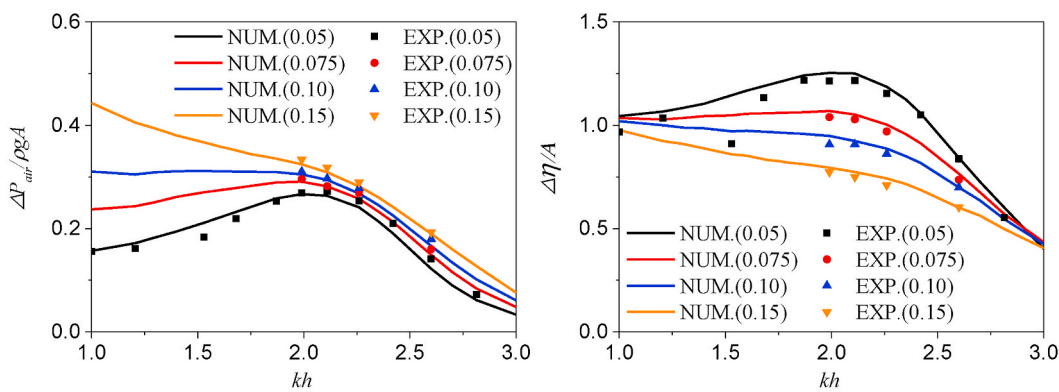


Fig. 11. Distributions of hydrodynamic efficiency ξ for different opening ratios ε of the air orifice, with the green dashed line indicating the efficiency of $\xi = 20\%$.

device is also considered for a direct comparison between the experimental and numerical investigations. In the physical tests, two different spring stiffness values are considered, i.e., $K_{33} = 25 \text{ kg/m}$ and 70 kg/m . The movement of the floating OWC device is restrained in the vertical direction. The main parameters are: $d = 0.3 \text{ m}$, $D = 0.8 \text{ m}$, $b_w = 0.1 \text{ m}$ and $\varepsilon = 3\%$. A series of monochromatic waves are generated with the wave steepness $kA = 0.05$. In the HOBEM model, the artificial and

nonlinear pneumatic damping coefficients are chosen to be $\mu_1 = 0.015$ and $\mu_2 = 1.45$, respectively. In Eqs. (20) and (21), the viscous scale factor v is set to 0.8.

Fig. 15 presents the variations of the vertical displacement of the floating OWC device with different mooring stiffness. It should be noted that some disagreement occurs for the case with stiffness $K_{33}=70 \text{ kg/m}$ in the high frequency region. It is due to the unstable spring stiffness, as K_{33} stands for an averaged stiffness in the experiment. The mooring stiffness plays a key role in the variations of the vertical displacement. The vertical displacement of the OWC device decreases with the increase of the mooring stiffness, especially for the low and intermediate frequency regions. As for the high frequency region, the amplitude of the vertical displacement is small in all cases. This is because the short waves with low energy fail to drive the motion with a large displacement. Fig. 16 shows the effects of the mooring stiffness on the hydrodynamic performance of the floating OWC chamber. The case of a stationary OWC device is also included. Fig. 16 illustrates good agreements between the HOBEM results and the experimental measurements. It can also be seen that the resonant frequency of the floating OWC system is the same as the stationary one. In Fig. 16(a) and (b), the amplitude of both the chamber air pressure P_{air} and the relative averaged surface elevation η_a increases with the mooring stiffness K_{33} in low and intermediate frequency regions. This is due to the vertical displacement of the OWC device partly cancels the air volume change inside the chamber, which leads to low air pressure. Within high frequency region ($kh \geq 2.5$), the air pressure P_{air} and the relative averaged surface elevation η_a of the floating device are larger than those of a fixed



(a) Amplitude of the chamber air pressure

(b) Amplitude of the averaged surface elevation

Fig. 12. Effects of the wave steepness kA on the hydrodynamic properties of the OWC chamber.

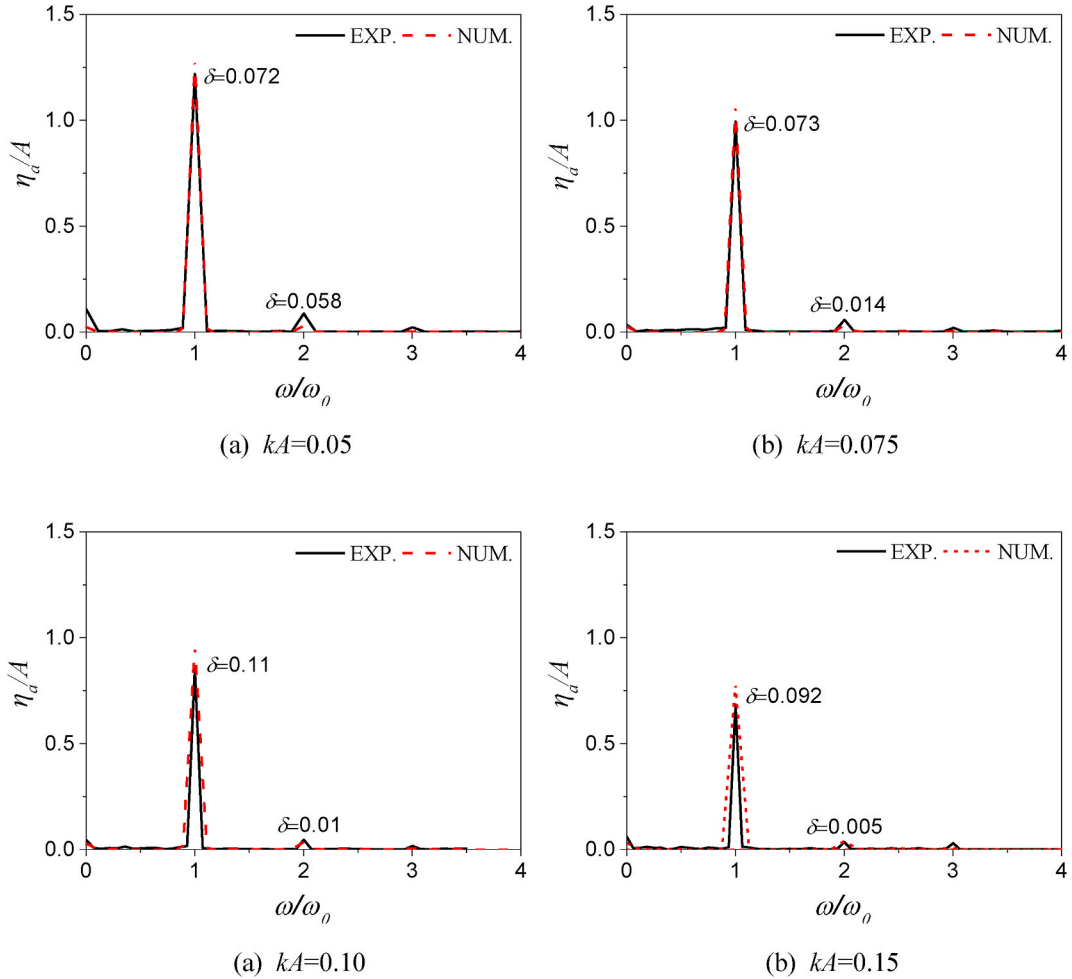


Fig. 13. Spectral analysis of the averaged chamber free surface elevation at $kh=2.11$.

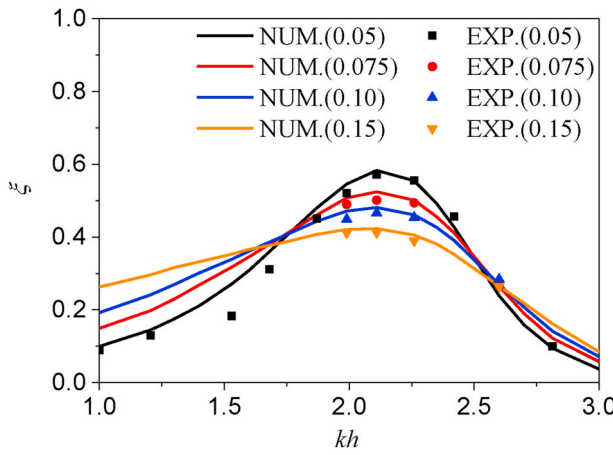


Fig. 14. Distributions of hydrodynamic efficiency ξ for different wave steepness kA .

OWC device. An opposite vertical motion occurs between the chamber and the water column inside the chamber, which enhances the volume flux inside the chamber with short waves. The effects of the mooring stiffness on the hydrodynamic efficiency, as shown in Fig. 16(c), follow the same trend as the air pressure P_{air} and the averaged surface elevation η_a . The resonant frequency occurs near the wave condition $kh = 2.1$, which is consistent with the air pressure P_{air} and the relative averaged

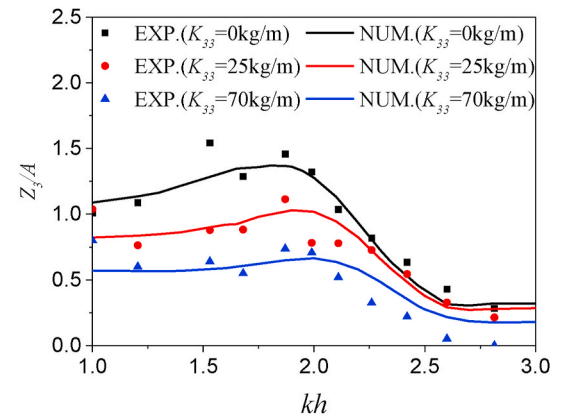


Fig. 15. Effects of the mooring line stiffness K_{33} on the vertical displacement Z_3 of the OWC chamber.

surface elevation η_a . The effective frequency bandwidth of the floating OWC device increases with the mooring stiffness, so the device can capture the wave energy in a wider frequency range.

5.4. Effects of the chamber draft

It is well known that the chamber draft has a significant influence on the hydrodynamic properties of the OWC device [67]. Two different

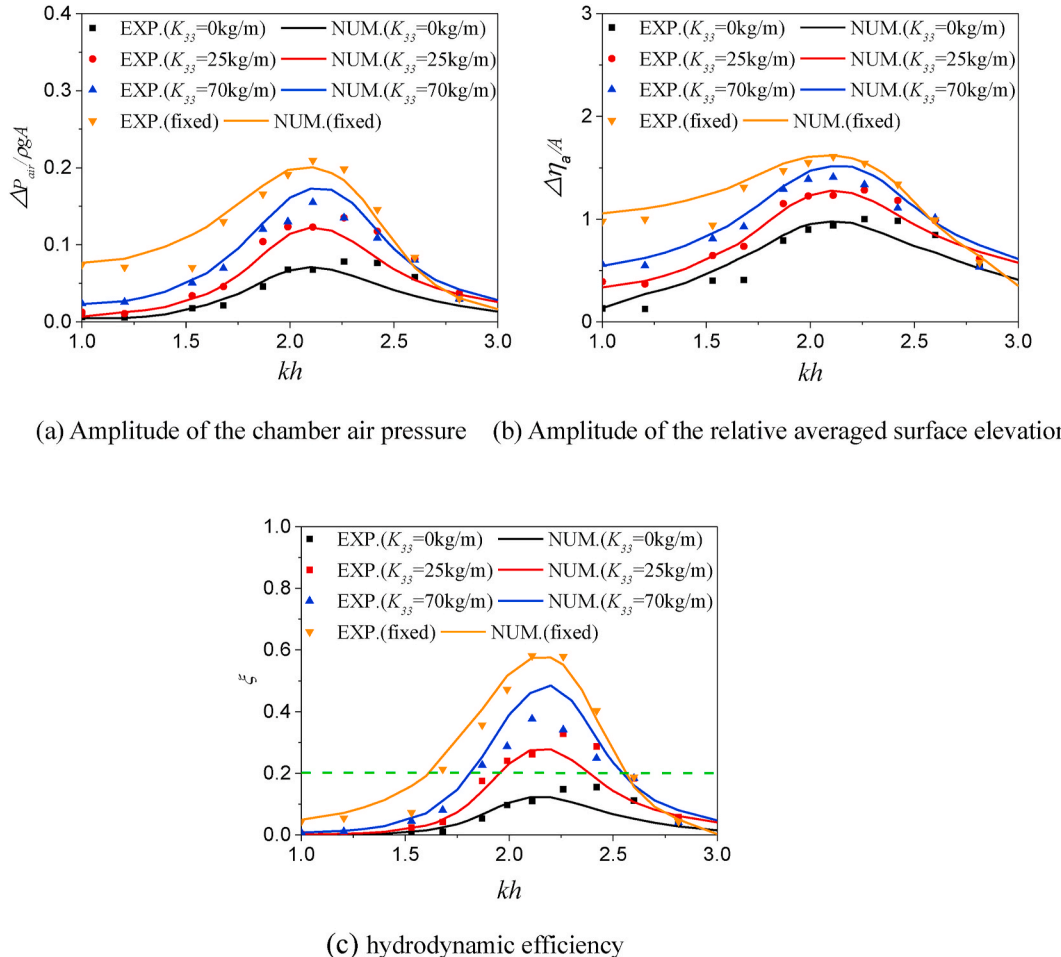


Fig. 16. Effects of the mooring stiffness on the hydrodynamic properties of the OWC chamber, with the green dashed line indicating the efficiency of $\xi = 20\%$.

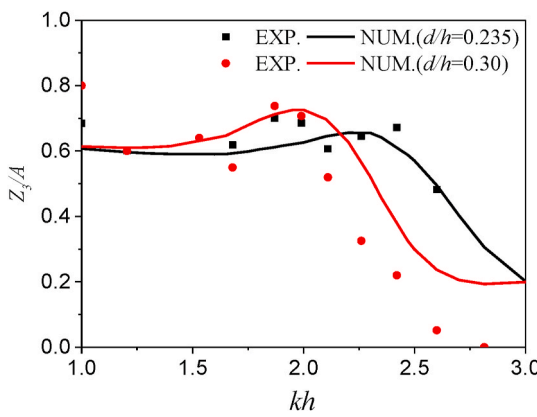


Fig. 17. Effects of the chamber draft d on the vertical displacement Z_3 of the OWC chamber.

OWC chamber drafts are studied, i.e., $d/h = 0.235$ and 0.30 . The mass of the OWC device increases from 52.84 kg to 67.45 kg as the chamber draft changes from 0.235 m to 0.3 m. Other main parameters are set as: $D = 0.8$ m, $b_w = 0.1$ m and $\varepsilon = 3\%$. The mooring stiffness K_{33} is selected as 70 kg/m. In the HOBEM model, the artificial and nonlinear pneumatic damping coefficients are chosen to be $\mu_1 = 0.015$ and $\mu_2 = 1.45$, respectively. The viscous scale factor v is set at 0.8 . The steepness of the incoming wave is set at $kA = 0.05$ within the wave frequency region $1 \leq kh \leq 3$.

The impacts of the draft d on the device performance are shown in Figs. 17 and 18. In Fig. 17, the vertical displacement of the device differs slightly between $d/h = 0.235$ and 0.3 in the low frequency region ($kh \leq 1.75$). Compared with the incident wave energy, the scattered wave energy, which is induced by the motion of the device, can be ignored in the low frequency region. The vertical displacement of the device with a larger chamber draft decreases rapidly at the high frequency region ($kh \geq 2.0$). Fig. 18 shows the amplitude variations of the hydrodynamic properties with chamber draft d as a function of the dimensionless wave number kh . It can be seen that the resonant frequency shifts to the higher one with the decrease of the chamber draft. Such a shift is due to the inertia of the OWC water column decreasing with the chamber draft [47]. The dimensionless amplitudes of the air pressure $\Delta P_{air}/\rho g A$, the relative averaged surface elevation $\Delta \eta_a/A$ and the hydrodynamic efficiency ξ decrease with the OWC chamber draft d at the resonant frequency. Comparing with a fixed OWC device [35], the resonant efficiency of the proposed floating device exhibits an opposite dependency on the chamber draft. Such a phenomenon can be explained that the vertical displacement of the OWC helps to cancel the air volume change induced by the chamber surface elevation. In Fig. 18(c), the effective frequency bandwidth Δkh corresponding to high operation efficiency $\xi \geq 20\%$ increases by 8% as the chamber draft decreases from 0.3 m to 0.235 m. In the high frequency region, a shallower chamber draft d leads to a higher hydrodynamic efficiency ξ . Fig. 18 also shows that the chamber draft can be changed to tune the device to suit different wave frequencies.

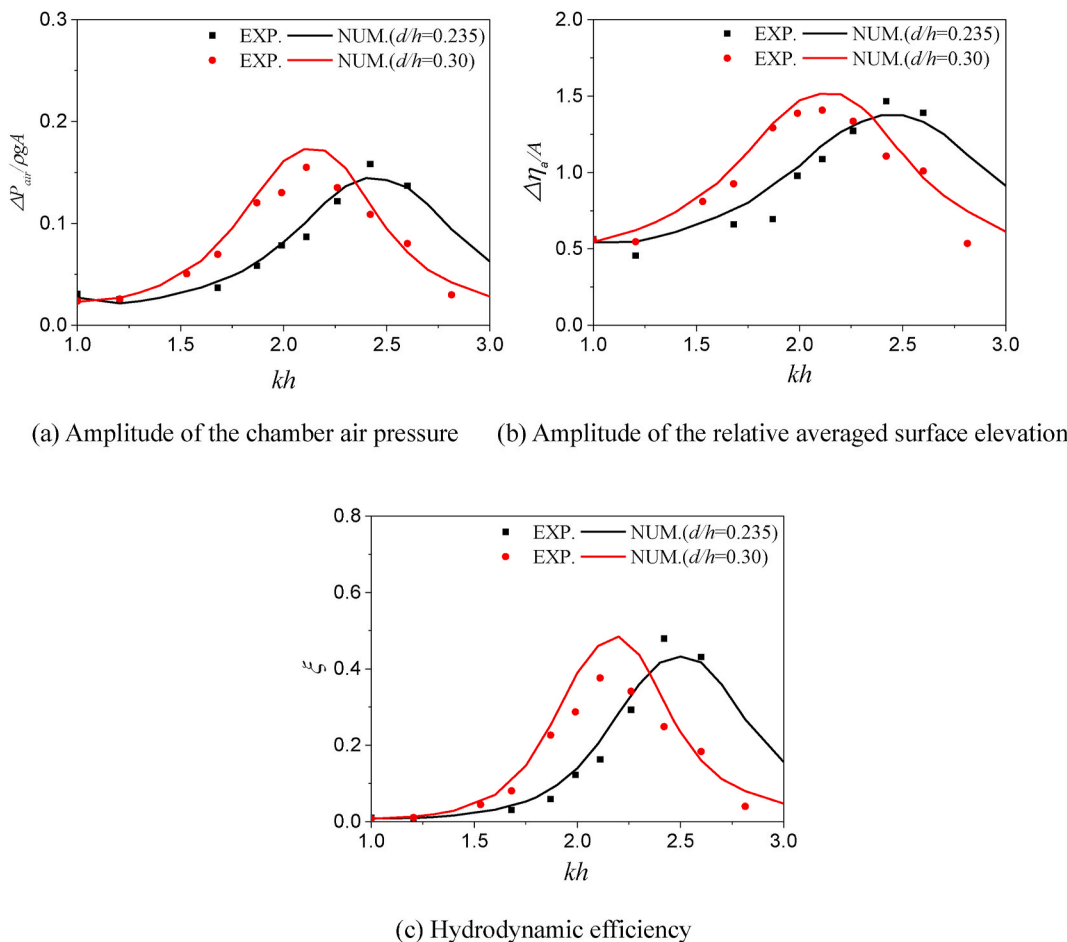


Fig. 18. Effects of the chamber draft d on the hydrodynamic properties of the OWC chamber.

6. Conclusions

In this study, the hydrodynamic performance of an offshore OWC wave energy converter is investigated experimentally and numerically. The experiment is carried out in the wave-current flume at the scale of 1:20. In order to systematically examine the energy conversion performance, the second-order time-domain HOBEM model is developed. The experimental data are used for validating the numerical model. The numerical results show good agreement with the experimental data. The present HOBEM model can be used to study the optimum design of the floating OWC device.

Four different opening ratios are considered to investigate the effects of turbine damping. It is found that the optional opening ratio is between 2% and 3%. The effects of the wave nonlinearity, as quantified by wave steepness, on the amplitude of the chamber air pressure, the averaged surface elevation and the hydrodynamic efficiency are discussed in detail. The nondimensional amplitudes of the air pressure and the averaged surface elevation vary in opposite trends with the wave steepness. The hydrodynamic efficiency and the effective frequency bandwidth increase with the mooring stiffness regardless of the wave frequencies. For the proposed floating OWC device, a smaller chamber draft leads to a wider effective frequency bandwidth, but a reduction in the resonant efficiency and frequency.

The present study is conducted under regular wave conditions, whereas irregular waves exist in the real ocean environment. In the experiment study, the mooring line of the floating OWC device is simulated by two springs, and only the vertical displacement is considered. Further work will concentrate on the effects of the irregular waves on multiple-degree-of-freedom OWC devices.

Credit author statement

Yu Zhou: Conceptualization, Methodology, Software, Validation, Investigation, Writing – original draft. Dezhi Ning: Conceptualization, Resources, Supervision, Writing – review & editing. Dongfang Liang: Writing – review & editing. Shuqun Cai: Writing – review & editing.

Declaration of competing interest

The authors declare that they have no known competing financial interests or personal relationships that could have appeared to influence the work reported in this paper.

Acknowledgements

This work is supported by the National Natural Science Foundation of China (Nos. 51679036), Joint grant between NSFC and Royal Society (No. IEC\NSFC\191369) and the grant of Chinese Academy of Sciences (Grant No. ISEE2018PY05).

References

- [1] Wang L, Isberg J, Tedeschi E. Review of control strategies for wave energy conversion systems and their validation: the wave-to-wire approach. *Renew Sustain Energy Rev* 2018;81:366–79.
- [2] Cruz J. Ocean wave energy: current status and future perspectives. Springer Science & Business Media; 2007.
- [3] Falnes J. A review of wave-energy extraction. *Mar Struct* 2007;20:185–201.
- [4] Hussain A, Arif SM, Aslam M. Emerging renewable and sustainable energy technologies: State of the art. *Renew Sustain Energy Rev* 2017;71:12–28.

- [5] Mahnamfar F, Altunkaynak A. Comparison of numerical and experimental analyses for optimizing the geometry of OWC systems. *Ocean Eng* 2017;130:10–24.
- [6] Zhao X, Ning D, Zou Q, Qiao D, Cai S. Hybrid floating breakwater-WEC system: a review. *Ocean Eng* 2019;186:106126.
- [7] Zabala I, Henriques J, Blanco J, Gomez A, Gato L, Bidaguren I, et al. Wave-induced real-fluid effects in marine energy converters: review and application to OWC devices. *Renew Sustain Energy Rev* 2019;111:535–49.
- [8] Falcão AF, Henriques JC. The spring-like air compressibility effect in oscillating-water-column wave energy converters: review and analyses. *Renew Sustain Energy Rev* 2019;112:483–98.
- [9] Nearshore Floating Oscillating Water Column: Prototype Development and Evaluation. UK: Department of Trade and Industry; 2005.
- [10] Falcão AF, Henriques JC, Cândido JJ. Dynamics and optimization of the OWC spar buoy wave energy converter. *Renew Energy* 2012;48:369–81.
- [11] Falcão AFO, Henriques JCC. Oscillating-water-column wave energy converters and air turbines: a review. *Renew Energy* 2016;85:1391–424.
- [12] López I, Carballo R, Taveira-Pinto F, Iglesias G. Sensitivity of OWC performance to air compressibility. *Renew Energy* 2020;145:1334–47.
- [13] Antonio FD-O. Wave energy utilization: a review of the technologies. *Renew Sustain Energy Rev* 2010;14:899–918.
- [14] Pawitan KA, Dimakopoulos AS, Vicinanza D, Allsop W, Bruce T. A loading model for an OWC caisson based upon large-scale measurements. *Coast Eng* 2019;145:1–20.
- [15] Ning DZ, Wang RQ, Chen LF, Sun K. Experimental investigation of a land-based dual-chamber OWC wave energy converter. *Renew Sustain Energy Rev* 2019;105:48–60.
- [16] Moretti G, Malara G, Scialò A, Daniele L, Romolo A, Vertechy R, et al. Modelling and field testing of a breakwater-integrated U-OWC wave energy converter with dielectric elastomer generator. *Renew Energy* 2020;146:628–42.
- [17] Xu C, Huang Z. Three-dimensional CFD simulation of a circular OWC with a nonlinear power-takeoff: model validation and a discussion on resonant sloshing inside the pneumatic chamber. *Ocean Eng* 2019;176:184–98.
- [18] Zheng S, Antonini A, Zhang Y, Greaves D, Miles J, Iglesias G. Wave power extraction from multiple oscillating water columns along a straight coast. *J Fluid Mech* 2019;878:445–80.
- [19] Zheng S, Zhang Y, Iglesias G. Coast/breakwater-integrated OWC: a theoretical model. *Mar Struct* 2019;66:121–35.
- [20] Doyle S, Aggidis GA. Development of multi-oscillating water columns as wave energy converters. *Renew Sustain Energy Rev* 2019;107:75–86.
- [21] Gomes RPF, Henriques JCC, Gato LMC, Falcão AFO. Wave power extraction of a heaving floating oscillating water column in a wave channel. *Renew Energy* 2016;99:1262–75.
- [22] Gomes R, Henriques J, Gato L, Falcão A. Time-domain simulation of a slack-moored floating oscillating water column and validation with physical model tests. *Renew Energy* 2020;149:165–80.
- [23] Oikonomou C, Gomes R, Gato L, Falcão A. On the dynamics of an array of spar-buoy oscillating water column devices with inter-body mooring connections. *Renew Energy* 2020;148:309–25.
- [24] Elhanafi A, Macfarlane G, Fleming A, Leong Z. Experimental and numerical investigations on the hydrodynamic performance of a floating-moored oscillating water column wave energy converter. *Appl Energy* 2017;205:369–90.
- [25] Sheng W. Power performance of BBDB OWC wave energy converters. *Renew Energy* 2019;132:709–22.
- [26] Howe D, Nader J-R. OWC WEC integrated within a breakwater versus isolated: experimental and numerical theoretical study. *International journal of marine energy* 2017;20:165–82.
- [27] Penalba M, Giorgi G, Ringwood JV. Mathematical modelling of wave energy converters: a review of nonlinear approaches. *Renew Sustain Energy Rev* 2017;78:1188–207.
- [28] He F, Zhang H, Zhao J, Zheng S, Iglesias G. Hydrodynamic performance of a pile-supported OWC breakwater: an analytical study. *Appl Ocean Res* 2019;88:326–40.
- [29] Zheng S, Zhu G, Simmonds D, Greaves D, Iglesias G. Wave power extraction from a tubular structure integrated oscillating water column. *Renew Energy* 2020;150:342–55.
- [30] Nader J-R, Zhu S-P, Cooper P. Hydrodynamic and energetic properties of a finite array of fixed oscillating water column wave energy converters. *Ocean Eng* 2014;88:131–48.
- [31] Rezanejad K, Bhattacharjee J, Soares CG. Stepped sea bottom effects on the efficiency of nearshore oscillating water column device. *Ocean Eng* 2013;70:25–38.
- [32] Zhao X, Xue R, Geng J, Göteman M. Analytical investigation on the hydrodynamic performance of a multi-pontoon breakwater-WEC system. *Ocean Eng* 2021;220:108394.
- [33] Wilbert R, Sundar V, Sannasiraj S. Wave interaction with a double chamber oscillating water column device. *International Journal of Ocean & Climate Systems* 2013;4:21–40.
- [34] Singh U, Abdussamie N, Hore J. Hydrodynamic performance of a floating offshore OWC wave energy converter: an experimental study. *Renew Sustain Energy Rev* 2020;117:109501.
- [35] Ning D-z, Zhou Y, Mayon R, Johanning L. Experimental investigation on the hydrodynamic performance of a cylindrical dual-chamber Oscillating Water Column device. *Appl Energy* 2020;260:114252.
- [36] Ashlin SJ, Sannasiraj S, Sundar V. Performance of an array of oscillating water column devices integrated with an offshore detached breakwater. *Ocean Eng* 2018;163:518–32.
- [37] Shalby M, Elhanafi A, Walker P, Dorrell DG. CFD modelling of a small-scale fixed multi-chamber OWC device. *Appl Ocean Res* 2019;99:37–47.
- [38] Dai S, Day S, Yuan Z, Wang H. Investigation on the hydrodynamic scaling effect of an OWC type wave energy device using experiment and CFD simulation. *Renew Energy* 2019;142:184–94.
- [39] Simonetti I, Cappietti L, Elsafti H, Oumeraci H. Evaluation of air compressibility effects on the performance of fixed OWC wave energy converters using CFD modelling. *Renew Energy* 2018;119:741–53.
- [40] Connell KO, Thiebaut F, Kelly G, Cashman A. Development of a free heaving OWC model with non-linear PTO interaction. *Renew Energy* 2018;117:108–15.
- [41] Koo W, Kim MH. Nonlinear time-domain simulation of a land-based oscillating water column. *J Waterw Port, Coast Ocean Eng* 2010;136:276–85.
- [42] Wang RQ, Ning DZ, Zhang CW, Zou QP, Liu Z. Nonlinear and viscous effects on the hydrodynamic performance of a fixed OWC wave energy converter. *Coast Eng* 2018;131:42–50.
- [43] Yang M, Teng B, Ning D, Shi Z. Coupled dynamic analysis for wave interaction with a truss spar and its mooring line/riser system in time domain. *Ocean Eng* 2012;39:72–87.
- [44] Medina-Lopez E, Ferrando AM, Gilabert MC, Pino Cd, Rodríguez ML. Note on a real gas model for OWC performance. *Renew Energy* 2016;85:588–97.
- [45] Soares CG. Offshore structure modelling. World Scientific1995.
- [46] Elhanafi A, Macfarlane G, Fleming A, Zhi L. Investigations on 3D effects and correlation between wave height and lip submergence of an offshore stationary OWC wave energy converter. *Appl Ocean Res* 2017;64:203–16.
- [47] Ning DZ, Wang RQ, Zou QP, Teng B. An experimental investigation of hydrodynamics of a fixed OWC Wave Energy Converter. *Appl Energy* 2016;168:636–48.
- [48] Ning DZ, Shi J, Zou QP, Teng B. Investigation of hydrodynamic performance of an OWC (oscillating water column) wave energy device using a fully nonlinear HOBEM (higher-order boundary element method). *Energy* 2015;83:177–88.
- [49] Morris-Thomas MT, Irvin RJ, Thiagarajan KP. An investigation into the hydrodynamic efficiency of an oscillating water column. *J Offshore Mech Arctic Eng* 2007;129:273–8.
- [50] Nader J-R, Zhu S-P, Cooper P, Stappenbelt B. A finite-element study of the efficiency of arrays of oscillating water column wave energy converters. *Ocean Eng* 2012;43:72–81.
- [51] Elhanafi A, Macfarlane G, Fleming A, Leong Z. Scaling and air compressibility effects on a three-dimensional offshore stationary OWC wave energy converter. *Appl Energy* 2017;189:1–20.
- [52] Bai W, Teng B. Simulation of second-order wave interaction with fixed and floating structures in time domain. *Ocean Eng* 2013;74:168–77.
- [53] Jin R, Teng B, Ning D, Zhao M, Cheng L. Numerical investigation of influence of wave directionality on the water resonance at a narrow gap between two rectangular barges. *Acta Oceanol Sin* 2017;36:104–11.
- [54] Farrant P. Three dimensional unsteady wave-body interactions by a rankine boundary element method. *Ship Technol Res* 1993;40:165–75.
- [55] Kim Y. Artificial damping in water wave problems I: constant damping. *Int J Offshore Polar* 2003;13.
- [56] Isaacson M, Cheung KF. Time-domain second-order wave diffraction in three dimensions. *J Waterw Port, Coast Ocean Eng* 1992;118:496–516.
- [57] Sheng W, Alcorn R, Lewis A. On thermodynamics in the primary power conversion of oscillating water column wave energy converters. *J Renew Sustain Energy* 2013;5:1257–94.
- [58] Isaacson M, Ng JY, Cheung KF. Second-order wave radiation of three-dimensional bodies by time-domain method. *Int J Offshore Polar* 1993;3.
- [59] Adhikari S, Phani AS. Experimental identification of generalized proportional viscous damping matrix. *J Vib Acoust* 2009;131.
- [60] Brito M, Canellas R, García-Feal O, Domínguez J, Crespo A, Ferreira R, et al. A numerical tool for modelling oscillating wave surge converter with nonlinear mechanical constraints. *Renew Energy* 2020;146:2024–43.
- [61] Zhou Y, Zhang C, Ning D. Hydrodynamic investigation of a concentric cylindrical OWC wave energy converter. *Energies* 2018;11:985.
- [62] Iturrioz A, Guanche R, Lara J, Vidal C, Losada I. Validation of OpenFOAM® for oscillating water column three-dimensional modeling. *Ocean Eng* 2015;107:222–36.
- [63] Sheng W, Flannery B, Lewis A, Alcorn R. Experimental Studies of a Floating Cylindrical OWC WEC. 31st International Conference on Ocean, Offshore and Arctic Engineering. Brazil: ASME. Rio de Janeiro; 2012. p. 169–78.
- [64] Zhou Y, Ning D, Shi W, Johanning L, Liang D. Hydrodynamic investigation on an OWC wave energy converter integrated into an OWT monopile. *Coast Eng* 2020;103731.
- [65] López I, Pereiras B, Castro F, Iglesias G. Performance of OWC wave energy converters: influence of turbine damping and tidal variability. *Int J Energy Res* 2015;39:472–83.
- [66] Kamath A, Bihs H, Arntsen ØA. Numerical modeling of power take-off damping in an oscillating water column device. *International Journal of Marine Energy* 2015;10:1–16.
- [67] Ning D, Zhou Y, Zhang C. Hydrodynamic modeling of a novel dual-chamber OWC wave energy converter. *Appl Ocean Res* 2018;78:180–91.